

Host Galaxy Line Diagnostics for the Candidate Tidal Disruption Events XMMSL1 J111527.3+180638 and PTF09axc

Anne Inkenhaag,^{1,2*} Peter G. Jonker,^{1,2} Giacomo Cannizzaro,^{1,2} Daniel Mata Sánchez,³ Richard D. Saxton⁴

¹*Department of Astrophysics/IMAPP, Radboud University Nijmegen, P.O. Box 9010, 6500 GL Nijmegen, The Netherlands*

²*SRON, Netherlands Institute for Space Research, Sorbonnelaan 2, 3584 CA, Utrecht, The Netherlands*

³*Jodrell Bank Centre for Astrophysics, Department of Physics and Astronomy, The University of Manchester, M13 9PL, UK*

⁴*Telespazio for ESA, XMM-Newton SOC, ESAC, Apartado 78, 28691 Villanueva de la Cañada, Madrid, Spain*

Accepted XXX. Received YYY; in original form ZZZ

ABSTRACT

We present results of our analysis of spectra of the host galaxies of the candidate Tidal Disruption Events (TDEs) XMMSL1 J111527.3+180638 and PTF09axc to determine the nature of these transients. We subtract the starlight component from the host galaxy spectra to determine the origin of the nuclear emission lines. Using a Baldwin–Phillips–Terlevich (BPT) diagram we conclude that the host galaxy of XMMSL1 J111527.3+180638 is classified as a Seyfert galaxy, suggesting this transient is likely to be caused by (extreme) variability in the active galactic nucleus. We find that the host of PTF09axc falls in the ‘star-forming’ region of the BPT-diagram, implying that the transient is a strong TDE candidate. For both galaxies we find a *WISE*-colour difference of $W1 - W2 < 0.8$, which means there is no indication of a dusty torus and therefore an active galactic nucleus, seemingly contradicting our BPT finding for the host of XMMSL1 J111527.3+180638. We discuss possible reasons for the discrepant results obtained through the two methods.

Key words: transients: tidal disruption events – galaxies: individual: NGC 3599 – galaxies: active – galaxies: nuclei – black hole physics

1 INTRODUCTION

Two-body relaxation processes in the nucleus of a galaxy make stars wander in energy and momentum space. This can bring the pericentre of a star’s orbit within its tidal radius (or Roche limit) given the supermassive black hole (SMBH) in the centre of the galaxy, causing the difference in gravitational pull between the part of the star nearest and furthest from the SMBH, also known as the tidal force, to overcome the self-gravity of the star. This results in the star being pulled apart in a tidal disruption event (TDE) (Hills 1975; Rees 1988; Phinney 1989).

Part of the stellar material of the disrupted star will stay bound to the SMBH and accrete on to it, creating a luminous flare that is visible across the electromagnetic spectrum (Rees 1988; Lodato & Rossi 2011). Over the last two decades, dozens of TDEs have been classified from among transient nuclear flares detected in X-ray, optical or UV (see Van Velzen et al. 2020; Saxton et al. 2021 for a review). Optically detected TDEs often go undetected in X-rays (Gezari et al. 2012), and vice versa. Although, there are events that have been found to emit in optical and X-rays (e.g., ASASSN-14li, ASASSN-15oi, AT 2019dsg, AT 2018fyk; Holoien et al. 2016; Gezari et al. 2017; Cannizzaro et al. 2021; Wevers et al. 2019, respectively).

A list of properties need to be satisfied for both optical/UV and X-ray selected TDE candidates to be confirmed. This list is based on observational characteristics shared by the known population of TDEs, and it is refined over time (see Zabludoff et al. 2021 for a

review). Key observables for optical/UV TDEs include broad He and/or H lines and blue continuum emission (see Van Velzen et al. 2020 for a review). A short rise to peak, steady decline and a soft X-ray spectrum are among the key observables for X-ray selected TDEs (see Saxton et al. 2021 for a review). There are multiple competing models explaining the optical-UV emission mechanism: outflows (photon-driven, Strubbe & Quataert 2009, line-driven, Miller 2015 or circularisation-driven, Metzger & Stone 2016), reprocessing of accretion disc emission by material in the debris stream at larger radii (Guillochon et al. 2014) or shocks in the self-intersecting debris stream (Piran et al. 2015; Bonnerot et al. 2017). The lack of agreement about the importance of, for instance, the self-intersection shock, the rate of circularisation of the stellar debris, and the accretion radiation efficiency makes that there is no single theoretical prediction that can serve as a guideline to classify an event as a TDE. While some of the observed properties can be explained by the theoretical models under consideration, there might be TDEs that do not fit in the sample of previously classified TDEs, for instance if they occupy a different part of the parameter space such as penetration factor (β), SMBH mass or spin, or stellar mass. Therefore, we need to keep a critical but open mind about which transients we classify as TDEs.

TDEs are often detected in otherwise inactive galaxies. However, Kennedy et al. (2016) suggest the TDE rate in AGNs could be enhanced with a factor up to 10 due to the interaction of stars with the disc around the AGN. Detecting TDEs in galaxies hosting an active galactic nucleus (AGN) is difficult, due to the inherent difficulty in distinguishing them from regular AGN activity, although some TDEs have been discovered in low-luminosity AGNs (e.g.,

* E-mail: a.inkenhaag@astro.ru.nl

ASASSN-14li and AT2019qiz; [Holoien et al. 2016](#); [Nicholl et al. 2020](#), respectively) and even higher luminosity AGNs (e.g., PS16dtm and SDSS J015957.64+003310.5; [Blanchard et al. 2017](#); [Merloni et al. 2015](#), respectively). When confronted with AGNs at the same redshift, TDEs are typically brighter ([Auchettl et al. 2018](#)), but more extreme AGN variability can be as luminous as a TDE flare (e.g., [Cannizzaro et al. 2020](#)). This emphasizes the difficulty in distinguishing between TDEs and AGN flares. Besides this, the interaction between the TDE debris stream and the AGN disc and the effect on the emitted luminosity are currently not well understood (although see [Chan et al. 2019, 2020](#) for modelling). Current theoretical models of the interaction of the stream originating in the destruction of a star and a pre-existing AGN disc are uncertain as they sample a restricted section of the parameter space and do not run long enough to study the accretion of an important fraction of the TDE debris. Finding a TDE candidate in a quiescent galaxy means there is one less alternative explanation for the transient.

A galaxy is classified as an AGN/non-quiescent galaxy if one or more of the following properties is observed ([Van Velzen et al. 2020](#)): *i*) The luminosity from the nucleus of the galaxy varied significantly with time before the main flare/transient event e.g., in the optical or X-ray luminosity, *ii*) The *WISE*-colours indicate the presence of a dusty torus, $W1 - W2 \geq 0.8$ ([Stern et al. 2012](#)), *iii*) The ratio between the equivalent widths (EWs) of specific emission lines in the optical – restframe – part of the nuclear host spectrum show that the source falls in the AGN region of the Baldwin–Phillips–Terlevich (BPT) diagram. The ratios of EWs of emission lines reflect the physical conditions under which these lines were formed. These conditions are different for the different options considered for their formations (e.g., AGN, star-forming regions, LINER-like shocks) ([Baldwin et al. 1981](#); [Cid Fernandes et al. 2010](#)). The AGN-region in the BPT-diagram is the region where the ionization-mechanism is dominated by the – UV / X-ray – ionizing radiation from the AGN ([Baldwin et al. 1981](#)).

In this work we investigate the host galaxy of two TDE candidates; the X-ray discovered TDE candidate XMMSL1 J111527.3+180638 in the galaxy NGC 3599 and the optically discovered candidate PTF09axc in the galaxy SDSS J145313.07+221432.2. The nature of the observed flare – AGN activity or TDE – has been subject of discussion in the literature for both of these candidates (e.g., [Saxton et al. 2015](#) for XMMSL1 J111527.3+180638 and [Arcavi et al. 2014](#); [Jonker et al. 2020](#) for PTF09axc).

We aim to classify the host galaxies of two TDE candidates by determining the position of the nuclear emission region on BPT-diagrams. We also look at the *WISE*-colours of the host galaxies and we use the existing $L_X \propto [\text{O III}]$ correlation observed in AGNs ([Heckman et al. 2005](#)) to compare the observed $[\text{O III}] \lambda 5007$ luminosity to what is predicted on the basis of the correlation. We finally compare the luminosity expressed in units of the Eddington luminosity of NGC 3599 with that of other low-luminosity AGN host galaxies of TDEs.

2 DATA

2.1 XMMSL1 J111527.3+180638

XMMSL1 J111527.3+180638 – XMMJ1115 from now on – was first reported as a candidate TDE based on an X-ray flare seen in *XMM-Newton* slew data on 2003 November 22 ([Esquej et al. 2007](#)). Its associated host galaxy is NGC 3599, at redshift $z = 0.0028$, $d_L = 19.86$ Mpc taken from the Cosmicflows-3 Distance Catalogue

([Tully et al. 2016](#)). Flux calibrated optical spectra were obtained from [Esquej et al. \(2008\)](#), originally [Caldwell et al. \(2003\)](#). This data set consists of two spectra: a blue spectrum with wavelengths 3500–5500 Å taken on 1998 May 20 and a red spectrum with wavelengths 5500–7500 Å taken on 2000 February 5, both taken at the F.L. Whipple Observatory (Mount Hopkins near Amado, Arizona, USA) with the FAST (FASt Spectrograph for the Tillinghast Telescope) instrument located on the 1.5-m Tillinghast telescope. Both spectra were taken before the reported X-ray flare (see [Caldwell et al. 2003](#) for full observational details and the data reduction procedure).

2.2 PTF09axc

PTF09axc was first reported by [Arcavi et al. \(2014\)](#) as part of their archival search of the Palomar Transient Factory (PTF) data for blue transients with $-21 \leq M_{R(\text{peak})} \leq -19$. The discovery date is 2009 June 20 and the source is associated with the galaxy SDSS J145313.07+221432.2 – hereafter SDSSJ1453 – at redshift $z = 0.115$ ([Arcavi et al. 2010](#)).

We have taken two 1800 s low resolution optical spectra of the nucleus of the host galaxy after the transient had faded ([Arcavi et al. 2014](#)) on 2019 July 14 and 15 using the Auxiliary-port CAMERA (ACAM) mounted at the Cassegrain focus of the William Herschel Telescope (WHT) located at the Roque de los Muchachos Observatory on La Palma, Spain under program W19AN009. Using the V400 grating, GG395A order blocking filter, and the AUXCAM CCD results in a wavelength coverage of 3950–9400 Å and resolution $R \sim 430$ for a 1 arcsec slit. We correct for instrumental broadening during the analysis of these data.

Data reduction is done using a program written in PYTHON that uses LACOSMIC ([Van Dokkum 2001](#)) for cosmic ray cleansing, PYRAF for bias and flatfield corrections and MOLLY, developed by T. Marsh ([Marsh 2019](#))¹, for wavelength calibrations. We further use MOLLY to flux calibrate and average our spectra.

3 ANALYSIS AND RESULTS

To obtain an accurate nuclear source classification we start by subtracting the starlight component from the host galaxy spectrum using the Penalized PiXel-Fitting (PPXF) method ([Cappellari 2017](#)), used with the MILES stellar library ([Vazdekis et al. 2010](#)). We use a degree four multiplicative Legendre polynomial – as opposed to an additive polynomial – to correct the continuum shape during the fit to prevent changes in the line strength of the absorption features in the templates, to minimize the influence on the strength of any emission line in the nuclear spectrum after subtraction. After subtraction the continuum emission is reduced to zero which means the equivalent width – flux in a line divided by the continuum – becomes undefined. Instead, we use the flux of the emission lines to determine the source position in a BPT-diagram. We use the python package LMFIT to fit Gaussian curves to the stellar-host subtracted emission – or absorption – lines to obtain the flux of the following emission lines of interest for the BPT-diagram(s), where present: $\text{H } \alpha$ $\lambda 6563$, $\text{H } \beta$ $\lambda 4861$, $[\text{O III}] \lambda 4959$, 5007 , $[\text{O I}] \lambda 6300$, $[\text{N II}] \lambda 6548$, 6584 , $[\text{S II}] \lambda 6617$, 6631 . To reduce the number of degrees of freedom during fitting we require the Full Width at Half Maximum (FWHM) of lines in doublets to be the same. We also fix the wavelength separation of doublets to their laboratory value and we fix the ratio in

¹ <http://deneb.astro.warwick.ac.uk/phsaap/software/molly/html/INDEX.html>

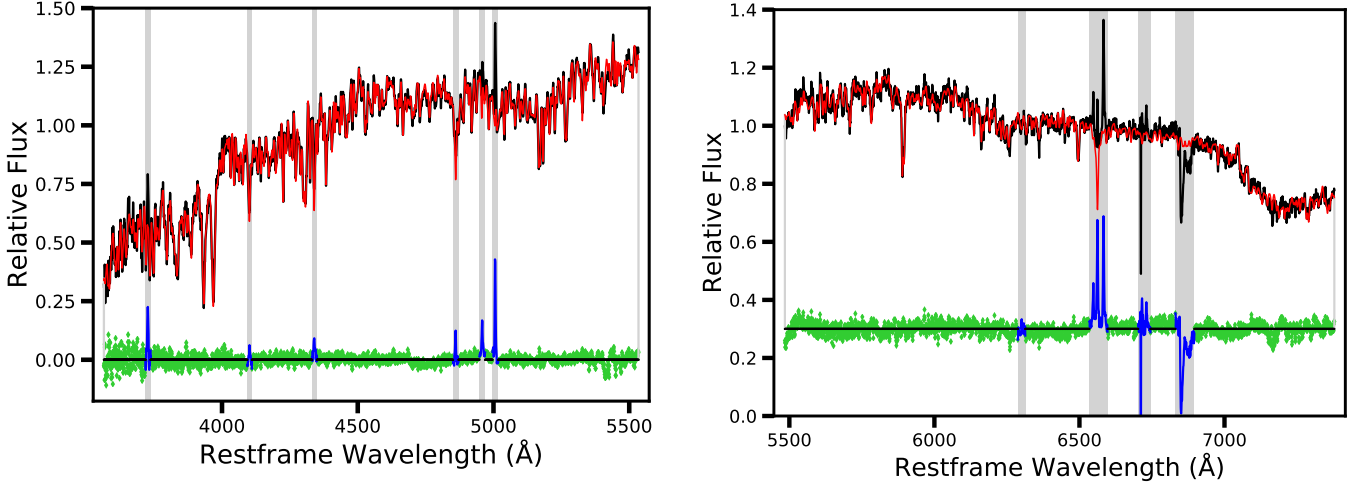


Figure 1. The normalised spectrum of NGC 3599 – host of XMMJ1115 – is shown in black, the best fit for the starlight component from `PPXF` is over-plotted in red, and the residuals after subtracting the best-fitting host-galaxy stellar spectrum is shown in green and blue. The grey bands – corresponding to the blue wavelength regions in the subtracted spectrum – are wavelengths around relevant host galaxy emission lines or telluric absorption lines expected from the night sky and they are therefore excluded from the `PPXF` fit. *Left panel:* The blue part of the spectrum (3500–5500 Å) displaying the masked emission lined from $H\beta$ $\lambda 4861$ and the $[O\text{III}]\lambda 4959, 5007$ doublet in grey. *Right panel:* The red part of the spectrum (5500–7500 Å) displaying the masked emission lines from $H\alpha$ $\lambda 6563$, the $[N\text{II}]\lambda 6548, 6584$ doublet and the $[S\text{II}]\lambda 6617, 6631$ doublet in grey. The region around $[O\text{I}]\lambda 6300$ is also masked, but there is no emission line detected when trying to fit a Gaussian at this wavelength.

amplitudes for the lines in doublets when an amplitude ratio is known ($[O\text{III}]\lambda 5007/[O\text{III}]\lambda 4959 = 3$ and $[N\text{II}]\lambda 6584/[N\text{II}]\lambda 6548 = 3$ from Osterbrock & Ferland 2006).

3.1 XMMJ1115

Fig. 1 shows the normalised – divided by the median value – galaxy spectrum in black, with the best fit from `PPXF` over-plotted in red, the grey bands represent areas masked during the fitting procedure. The red and blue parts, as described in Section 2.1, of the spectrum are fitted separately. The best fitting stellar population has a redshifted radial velocity of $799 \pm 2 \text{ km s}^{-1}$ (we average the radial velocity derived from the red and the blue parts of the spectrum). Taking into account the average rms uncertainty of 58 km s^{-1} on the wavelength calibration (from Caldwell et al. 2003) the redshift we derive is in agreement with previous measurements for this galaxy (e.g., $839 \pm 5 \text{ km s}^{-1}$; Cappellari et al. 2011). Subtracting the starlight component leaves us with the nuclear emission line spectrum (blue/green in Fig. 1).

We detect emission lines of $H\alpha$, $H\beta$ and the $[O\text{III}]$, $[N\text{II}]$ and $[S\text{II}]$ doublets, but we do not detect a significant emission line for $[O\text{I}]$ in this source. The detected emission lines are best fitted with one Gaussian component with an average FWHM of $253 \pm 9 \text{ km s}^{-1}$ (see Table A1 in the appendix). We provide figures showing the Gaussian fits to the detected emission lines in Fig. A1 in the appendix.

Using the flux of the emission lines we calculate the position of the source in a BPT-diagram. We use the demarcations from Kewley et al. (2001); Kauffmann et al. (2003); Kewley et al. (2006) to indicate different ionization-mechanism regions. The location of NGC3599 in the BPT-diagram is shown in Fig. 2 and it is consistent with an AGN/Seyfert classification for the spectrum of the nuclear region of the host of XMMJ1115.

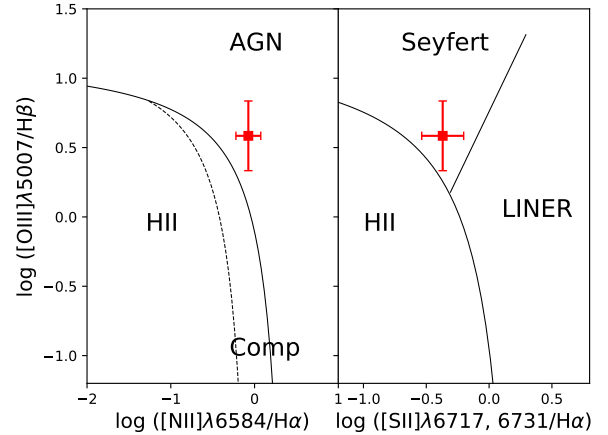


Figure 2. Baldwin–Phillips–Terlevich (BPT) diagram (Baldwin et al. 1981) for the nucleus of NGC 3599 derived using the flux measurements of the emission lines detected in the pre-outburst spectrum. The left panel uses the ratio between the $[O\text{III}]\lambda 5007$ and the $H\beta$ emission line flux and the ratio between the $[N\text{II}]\lambda 6584$ and the $H\alpha$ emission line flux while the left panel used the ratio between the $[O\text{III}]\lambda 5007$ and $H\beta$ emission line flux and the ratio between the $[S\text{II}]\lambda 6617, 6731$ and $H\alpha$ emission line flux. The demarcations between different regions caused by different ionization mechanisms are from Kewley et al. (2001); Kauffmann et al. (2003); Kewley et al. (2006). The position of the source in both diagrams is consistent with an AGN/Seyfert galaxy being present in NGC 3599 prior to the flare.

3.2 PTF09axc

We repeat the exact same data analysis procedure we employed for NGC 3599 for the host of PTF09axc (SDSSJ1453), see Section 3.1. Blueshifting the spectrum with $z = 0.1153$ before using `PPXF` leaves a residual radial velocity of $9 \pm 21 \text{ km s}^{-1}$, which is consistent

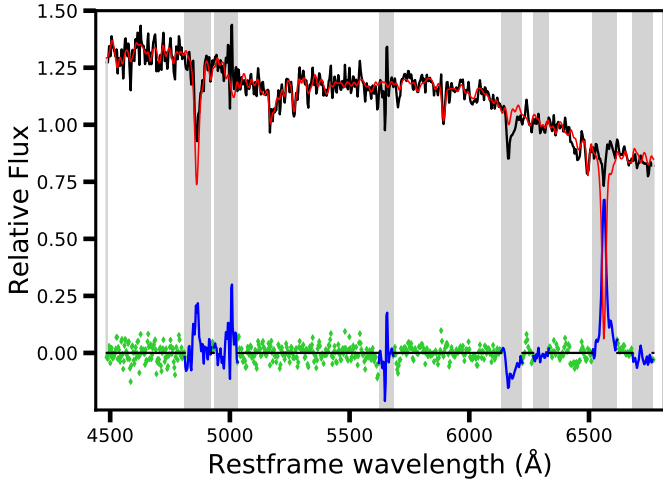


Figure 3. The normalised spectrum of SDSSJ1453 – host of PTF09axc – with the same colour scheme as in Fig. 1. The masked emission lines in grey are H α λ 6563, H β λ 4861, the [O III] λ 4959, 5007 doublet and the [N II] λ 6548, 6584 doublet. pPXF also masks [O I] λ 6300 and [S II] λ 6617, 6631, but there are no visible emission lines present in the subtracted spectrum at those wavelengths.

with no residual radial velocity. Therefore, the best-fitting stellar population has redshift of $z = 0.1153 \pm 0.0001$, corresponding to radial velocity $32590 \pm 30 \text{ km s}^{-1}$. For an uncertainty in the last digit of the redshift given in Arcavi et al. (2010) (confirmed through private communication) as small as 1, our values are completely consistent with their redshift. This redshift corresponds to $d_L = 536.1 \text{ Mpc}$ using $\Omega_m = 0.3$, $\Omega_\Lambda = 0.7$ and $H_0 = 70 \text{ km s}^{-1} \text{ Mpc}^{-1}$.

We do not detect emission lines for [O I] and the [S II] doublet, but we do detect the [N II] doublet and the H α and H β emission lines. To ensure the Gaussian functions fit to H α and the [N II] doublet have the correct central wavelength, we have to fix the wavelength separation between the lines. We fit a single component with an (average) FWHM = $768 \pm 102 \text{ km s}^{-1}$ to the detected emission lines. We derive an upper limit to the flux for both lines in the [O III] doublet.

Due to the redshift of this source the [O III] λ 5007 emission line is redshifted to $\sim 5584 \text{ \AA}$ which is close to the wavelength of the [O I] λ 5577 terrestrial sky emission line. In fact, these two lines fall within one ACAM resolution element of each other. In order to obtain as accurate as possible an upper limit on the presence of the [O III] λ 5007, we tried several data reduction optimisations tailored to allow as clean a subtraction of the terrestrial sky emission line as possible. To make sure the sky lines are perpendicular to the spectral trace we extracted a rectified version of the 2-D spectrum. This did not significantly improve the subtraction of the sky emission line. Next, we used the FIT2D option during the IRAF APALL procedure to extract the spectrum, which uses a two dimensional function to smooth the profile to use with variance weighting or cleaning. However, this also did not significantly improve the subtraction of the sky emission line either. Therefore, we proceed with the spectrum obtained from the original data reduction process, with the one difference that for determining the upper limit to the [O III] doublet emission line we do not subtract the sky emission lines.

Instead, we derive an upper limit for the flux in the [O III] λ 5007 line by fitting two Gaussians, one to the 5577 \AA sky line and one to the [O III] λ 5007 line. We shift the spectrum back to the rest frame

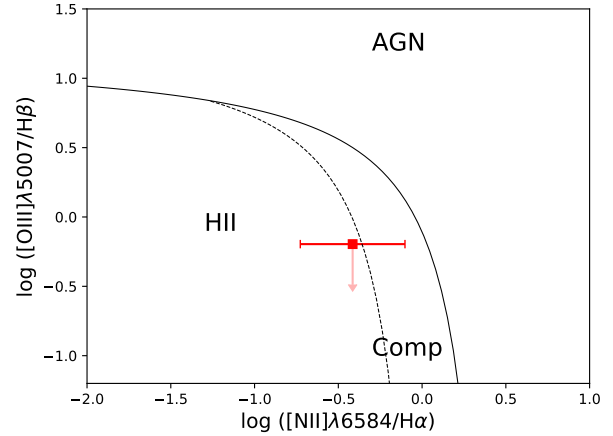


Figure 4. Baldwin–Phillips–Terlevich (BPT) diagram (Baldwin et al. 1981) using the flux measurements for the emission lines detected in the post-outburst spectrum of SDSSJ1453. It uses the ratio between the [O III] λ 5007 and H β emission line flux and the ratio between the [N II] λ 6584 and H α emission line flux. The position of the source is consistent with an H II/star forming region or a composite region within the error bars.

wavelength of the host galaxy, this includes the 5577 \AA sky line. We fix the central wavelength of the Gaussian function designed to describe this sky line to the expected value after blueshifting this line to the galaxy rest frame. In addition, we fix its FWHM to the spectral resolution of ACAM, leaving only the amplitude as a free parameter for this Gaussian during the fit. For the Gaussian designed to determine the upper limit to the [O III] λ 5007 line, we fix the central wavelength to where we expect it to appear. We fix the FWHM of this emission line to the average value measured in the other lines. This leaves only the amplitude as a free parameter in the fit for this Gaussian. We fit the [O III] λ 4959 line simultaneously, with the same FWHM as [O III] λ 5007 and the wavelength separation between the lines of the doublet set to the laboratory value, leaving only the amplitude free during the fit. As the upper limit on the flux of the Gaussian-shaped emission line is determined from a one sided Gaussian probability distribution, the 2σ upper limit corresponds to the 95 per cent confidence level. We use this upper limit to derive the position of the source in a BPT-diagram (see Fig. 4). The source falls in the region of the BPT-diagram associated with star-forming and H II galaxies.

4 DISCUSSION

In this paper we investigate the nature of two candidate TDE events, XMMJ1115 and PTF09axc, by classifying the nuclear regions of their host galaxies, NGC 3599 and SDSSJ1453, respectively. We apply two methods: optical emission lines ratios to assess the ionization-mechanism and the infrared (IR) colours as determined by the WISE-satellite (Wright et al. 2010) to investigate if dust, as often found in a dusty torus in an AGN, is present. The dusty torus of an AGN will yield $W1 - W2 \geq 0.8$ (Stern et al. 2012), where $W1$ and $W2$ indicate the WISE-bands at 3.4 and 4.6 \mu m , respectively. For SDSSJ1453, we apply a third method using the empirical relation between $L_X(3-20 \text{ keV})$ and $L_{[\text{O III}]}$ from Heckman et al. (2005) to assess if the observed X-ray luminosity is consistent with that from an AGN assuming the [O III] emission is caused by the AGNs narrow line region.

The position of NGC 3599 on the BPT-diagram suggests it is

a Seyfert galaxy, and there have been more papers suggesting the host galaxy is not a quiescent galaxy, see e.g., Saxton et al. (2015). Saxton et al. (2015) show that the galaxy was luminous in X-rays 18 months before the peak flux was measured, showing it to be bright on much longer timescales than shown by TDEs known at that point in time. They also argue that even if one of the two measurements was taken during rise-time and one during decay, the rise-time and the plateau phase together would still be significantly longer than seen in previous TDE candidates at that time. Since then, however, longer lived TDE-candidates have been observed (e.g., Lin et al. 2017) which means the measurements by Saxton et al. (2015) can no longer be considered unusual behaviour for a TDE. With our current understanding of X-ray TDE light curves we can therefore not make a definitive distinction between a TDE or AGN-activity for the flare XMMJ1115. However, our work does strengthen the evidence that the nucleus of NGC 3599 hosts a low-luminosity AGN.

We calculate $W1 - W2 = -0.032 \pm 0.029 < 0.8$, which means that, according to the *WISE*-colours, this source should not be classified as an AGN. This seemingly contradicts our findings that this source is a Seyfert galaxy given its position in the BPT-diagram. As *WISE* has a low spatial resolution (namely 6.1 arcsec, in band *W1* and 6.4 arcsec, in band *W2*), the *WISE*-colour will be a combination of the starlight of the galaxy plus that of the central Seyfert region of the galaxy. Additionally, LaMassa et al. (2019) found that not all AGN are detected by *WISE*, explaining that a non-detection of a known AGN in *WISE* is a possible result of different dust properties, or absence of dust, compared to AGN that are detected by *WISE*, rather than absence of the AGN. We therefore deem our result that NGC 3599 hosts a low-luminosity AGN based on the optical emission line ratios not to be in contradiction of the *WISE* non-detection. Our conclusion that the nuclear region of NGC 3599 hosts an actively accreting Seyfert-like AGN increases the probability that the observed flare was related to the AGN, although this does not rule out that the XMMJ1115 event was caused by a TDE interacting with the AGN accretion disc (Blanchard et al. 2017; Chan et al. 2019, 2020).

Assuming NGC 3599 is an AGN and using the empirical relation between $L_X(3-20 \text{ keV})$ and $L_{[\text{O III}]}$ for AGNs from Heckman et al. (2005), including the 1σ uncertainty in this relation and our 1σ uncertainty on the flux measurement, we calculate that $L_X(3-20 \text{ keV}) = 2.25^{+7.26}_{-1.77} \times 10^{41} \text{ erg s}^{-1}$ for NGC 3599. We use this to compute the Eddington ratio of this galaxy in quiescence and compare the value to the observed Eddington ratio of host galaxies of previously confirmed TDEs in low-luminosity AGNs, ASASSN-14li, IC3599 and AT2019qiz (Holoien et al. 2016; Campana et al. 2015; Nicholl et al. 2020, respectively). We list the observed $L_X(3-20 \text{ keV})$ values from the literature in Table 1, with the X-ray luminosities converted to the 3–20 keV energy band using W3PIMMS², as well as our calculated value for NGC 3599. The Eddington ratio calculated for NGC 3599 in quiescence is consistent with Eddington ratios found in other Seyfert galaxies within 1σ (see e.g., Singh et al. 2011). It is also consistent with the Eddington ratios of the host galaxies of known TDEs in low luminosity AGNs within 1σ , see Fig 5. There we plot the Eddington ratios for the different host galaxies as well as the range of Eddington ratios found by Singh et al. (2011). The uncertainty in the Eddington ratio for NGC 3599 is dominated by the uncertainty in our flux measurements, in the Heckman et al. (2005) relation and in the black hole mass estimate. Therefore, we favour the conclusion based on the position of the source in the BPT-diagram.

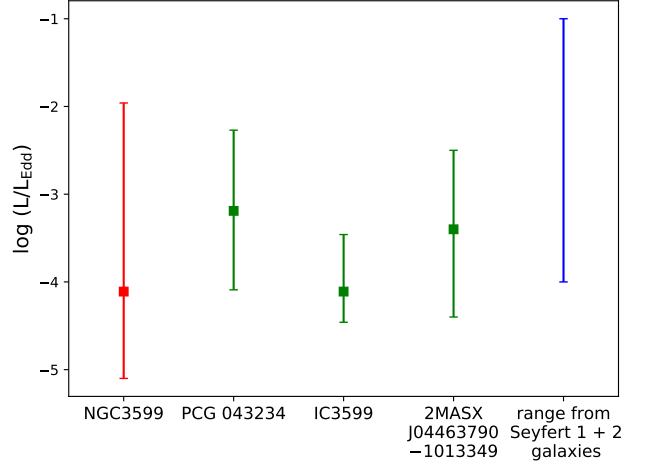


Figure 5. The Eddington ratio for X-ray luminosity of the nucleus three host galaxies of confirmed TDEs in low-luminosity AGNs is shown in green. Our measurement of the Eddington ratio for NGC 3599 based on the spectrum and using the relation from Heckman et al. (2005) to calculate the X-ray luminosity in the 3–20 keV band is shown in red. The blue range shows the Eddington ratios found in Seyfert 1 and Seyfert 2 galaxies by Singh et al. (2011) to represent the range in Eddington ratios for the population of Seyfert galaxies. For the masses, and luminosities used to calculate the Eddington ratio, see Table 1.

We do however note that this comparison of the Eddington ratios also does not exclude a TDE nature of the flare XMMJ1115.

The ratio of the flux of the emission lines in the optical spectrum of the nuclear region of SDSSJ1453 falls in the H II/starforming region, with the 1σ error bar extending into the composite galaxy region (see Fig. 4). The *WISE*-colour difference for SDSSJ1453 is $W1 - W2 = 0.15 \pm 0.08 < 0.8$, which does not indicate the presence of an AGN in this galaxy. As both the location of the source in a BPT-diagram as well as the *WISE*-colours indicate an inactive galaxy, we conclude that an AGN origin of the observed flare PTF09axc is unlikely, whereas a TDE nature of this transient is consistent with a quiescent galaxy.

Using the empirical relation between $L_X(3-20 \text{ keV})$ and $L_{[\text{O III}]}$ from Heckman et al. (2005) for AGNs (with a scatter of $\sigma = 0.51$ dex or a factor of ≈ 3.25) and $L_X = 8 \times 10^{42} \text{ erg s}^{-1}$ from Jonker et al. (2020), the predicted AGN luminosity from the [O III] line would be $L_{[\text{O III}]} \approx 5.7 \times 10^{40} \text{ erg s}^{-1}$. Using our 2σ upper limit for the flux in the emission line of $1.39 \times 10^{-16} \text{ erg cm}^{-2} \text{ s}^{-1}$ and $d_L = 536.1 \text{ Mpc}$ we calculate $L_{[\text{O III}]} = 4.78 \times 10^{39} \text{ erg s}^{-1}$, which is a factor 11.9 lower than expected for an AGN-powered emission line (see Figure 6 where we show the relation and our upper limit on $L_{[\text{O III}]}$). While our observed upper limit for the $L_{[\text{O III}]}$ is too low compared to the luminosity predicted by the correlation from Heckman et al. (2005), it is consistent if we take the uncertainty on this correlation into account within 3σ . This means we cannot exclude that the PTF09axc host SDSSJ1453 is an AGN, based on the $L_X \propto [\text{O III}]$ relation from Heckman et al. (2005). However, the combined evidence provided by the upper limit on $L_{[\text{O III}]}$, from the position of this source on the BPT-diagram, and the *WISE*-colour difference, we conclude that this galaxy is most likely quiescent and the transient PTF09axc is most likely a TDE.

It should be noted that in all low- to medium-resolution spectroscopic ground based observations the [O III] $\lambda 5007$ emission line in SDSSJ1453 is redshifted to fall close to the [O I] $\lambda 5577$ terrestrial

² <https://heasarc.gsfc.nasa.gov/cgi-bin/Tools/w3pimms/w3pimms.pl>

Table 1. X-ray luminosities, BH masses and Eddington ratios of host galaxies of known TDEs in low-luminosity AGNs and the host galaxy of XMMJ1115.

Transient name	Host galaxy name	$L_X(3-20 \text{ keV})$ (erg s^{-1})	BH mass (M_\odot)	$\log(L/L_{\text{Edd}})$	Reference
XMMJ1115	NGC 3599	$2.25^{+7.26}_{-1.77} \times 10^{41} *$	$2.34 \pm 2.27 \times 10^7$	$-4.11^{+2.15}_{-0.99}$	a
ASASSN-14li	PGC 043234	$1.32^{+3.09}_{-0.93} \times 10^{41}$	$1.70^{+2.47}_{-1.02} \times 10^6$	$-3.19^{+0.92}_{-0.90}$	b,c,d
–	IC3599	$6.73^{+1.96}_{-1.6} \times 10^{40}$	$7 \pm 5 \times 10^6$	$-4.11^{+0.65}_{-0.35}$	e, f, g
AT2019qiz	2MASX J04463790–1013349	$5.6^{+20.2}_{-4.7} \times 10^{40} *$	$1.15^{+0.85}_{-0.49} \times 10^6$	$-3.40^{+0.90}_{-1.0}$	h

Note. For IC3599 no transient name is listed as this host galaxy has seen multiple flares classified as TDEs since the early 1990s. L_X marked with * are calculated using the relation between $L_X(3-20 \text{ keV})$ and $L_{[\text{O III}]}$ from Heckman et al. (2005), while the other given values are observed L_X converted to the 3–20 keV band using W3PIMMS². References: a Saxton et al. (2015), b Miller et al. (2015), c Van Velzen et al. (2016), d Wevers et al. (2017), e Campana et al. (2015), f Grupe et al. (2001), g Grupe et al. (2015), h Nicholl et al. (2020)

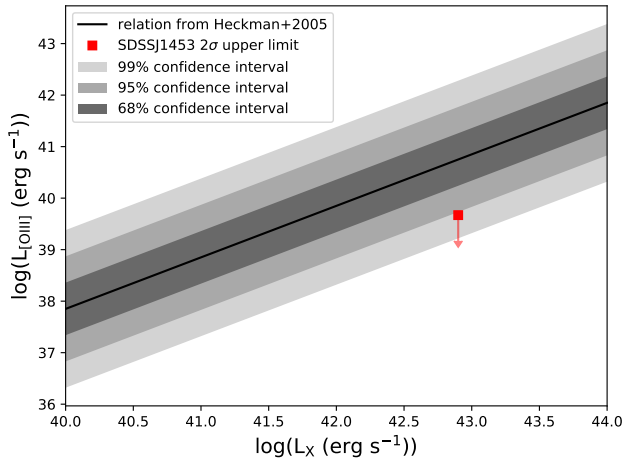


Figure 6. The empirical relation between $L_X(3-20 \text{ keV})$ and $L_{[\text{O III}]}$ for AGNs from Heckman et al. (2005) including the 1σ , 2σ and 3σ uncertainty regions on the relation in black and increasingly light shades of grey, respectively. In red is our 2σ upper limit on $L_{[\text{O III}]}$ combined with the measurement for $L_X(3-20 \text{ keV})$ from Jonker et al. (2020) to show our upper limit of the host of PTF09axc is not consistent with the relation within 2σ , but it is within 3σ .

sky line, although in previous work (e.g., Arcavi et al. 2014) there is no mention of this. Their $L_{[\text{O III}]}$ is consistent with our upper limit and not consistent with the empirical relation between $L_X(3-20 \text{ keV})$ and $L_{[\text{O III}]}$ and therefore supports our conclusion about PTF09axc.

ACKNOWLEDGEMENTS

D.M.S. acknowledges support from the ERC under the European Union’s Horizon 2020 research and innovation programme (grant agreement No. 715051; Spiders). This work is part of the research programme Athena with project number 184.034.002, which is financed by the Dutch Research Council (NWO). We thank Tom Marsh for the use of MOLLY. This work uses PYTHON packages NUMPY, LMFIT, MATPLOTLIB, SYS, ASTROPY.

DATA AVAILABILITY

All data will be made available in a reproduction package uploaded to Zenodo.

REFERENCES

- Arcavi I., et al., 2010, *ApJ*, **721**, 777
 Arcavi I., et al., 2014, *ApJ*, **793**, 38
 Auchettl K., Ramirez-Ruiz E., Guillochon J., 2018, *ApJ*, **852**, 37
 Baldwin J. A., Phillips M. M., Terlevich R., 1981, *PASP*, **93**, 5
 Blanchard P. K., et al., 2017, *ApJ*, **843**, 106
 Bonnerot C., Rossi E. M., Lodato G., 2017, *MNRAS*, **464**, 2816
 Caldwell N., Rose J. A., Concannon K. D., 2003, *AJ*, **125**, 2891
 Campana S., Mainetti D., Colpi M., Lodato G., D’Avanzo P., Evans P. A., Moretti A., 2015, *A&A*, **581**, A17
 Cannizzaro G., et al., 2020, *MNRAS*, **493**, 477
 Cannizzaro G., et al., 2021, *MNRAS*, **504**, 792
 Cappellari M., 2017, *MNRAS*, **466**, 798
 Cappellari M., et al., 2011, *MNRAS*, **413**, 813
 Chan C.-H., Piran T., Krolik J. H., Saban D., 2019, *ApJ*, **881**, 113
 Chan C.-H., Piran T., Krolik J. H., 2020, *ApJ*, **903**, 17
 Cid Fernandes R., Stasińska G., Schlickmann M. S., Mateus A., Vale Asari N., Schoenell W., Sodr e L., 2010, *MNRAS*, **403**, 1036
 van Dokkum P. G., 2001, *PASP*, **113**, 1420
 Esquej P., Saxton R. D., Freyberg M. J., Read A. M., Altieri B., Sanchez-Portal M., Hasinger G., 2007, *A&A*, **462**, L49
 Esquej P., et al., 2008, *A&A*, **489**, 543
 Gezari S., et al., 2012, *Nature*, **485**, 217
 Gezari S., Cenko S. B., Arcavi I., 2017, *ApJ*, **851**, L47
 Grupe D., Thomas H. C., Beuermann K., 2001, *A&A*, **367**, 470
 Grupe D., Komossa S., Saxton R., 2015, *ApJ*, **803**, L28
 Guillochon J., Manukian H., Ramirez-Ruiz E., 2014, *ApJ*, **783**, 23
 Heckman T. M., Ptak A., Hornschemeier A., Kauffmann G., 2005, *ApJ*, **634**, 161
 Hills J. G., 1975, *Nature*, **254**, 295
 Holoen T. W. S., et al., 2016, *MNRAS*, **455**, 2918
 Jonker P. G., Stone N. C., Generozov A., van Velzen S., Metzger B., 2020, *ApJ*, **889**, 166
 Kauffmann G., et al., 2003, *MNRAS*, **346**, 1055
 Kennedy G. F., Meiron Y., Shukirgaliyev B., Panamarev T., Berczik P., Just A., Spurzem R., 2016, *MNRAS*, **460**, 240
 Kewley L. J., Dopita M. A., Sutherland R. S., Heisler C. A., Trevena J., 2001, *ApJ*, **556**, 121
 Kewley L. J., Groves B., Kauffmann G., Heckman T., 2006, *MNRAS*, **372**, 961
 LaMassa S. M., Georgakakis A., Vivek M., Salvato M., Ananna T. T., Urry C. M., MacLeod C., Ross N., 2019, *ApJ*, **876**, 50
 Lin D., et al., 2017, *Nature Astronomy*, **1**, 0033
 Lodato G., Rossi E. M., 2011, *MNRAS*, **410**, 359
 Marsh T., 2019, molly: 1D astronomical spectra analyzer (ascl:1907.012)
 Merloni A., et al., 2015, *MNRAS*, **452**, 69
 Metzger B. D., Stone N. C., 2016, *MNRAS*, **461**, 948
 Miller M. C., 2015, *ApJ*, **805**, 83
 Miller J. M., et al., 2015, *Nature*, **526**, 542
 Nicholl M., et al., 2020, *MNRAS*, **499**, 482

- Osterbrock D. E., Ferland G. J., 2006, *Astrophysics of gaseous nebulae and active galactic nuclei*. Sausalito, CA: University Science Books
- Phinney E. S., 1989, in Morris M., ed., *The Center of the Galaxy*. Springer Netherlands, Dordrecht, pp 543–553
- Piran T., Svirski G., Krolik J., Cheng R. M., Shiokawa H., 2015, *ApJ*, **806**, 164
- Rees M. J., 1988, *Nature*, **333**, 523
- Saxton R. D., Motta S. E., Komossa S., Read A. M., 2015, *MNRAS*, **454**, 2798
- Saxton R., Komossa S., Auchettl K., Jonker P. G., 2021, *Space Sci. Rev.*, **217**, 18
- Singh V., Shastri P., Risaliti G., 2011, *A&A*, **533**, A128
- Stern D., et al., 2012, *ApJ*, **753**, 30
- Strubbe L. E., Quataert E., 2009, *MNRAS*, **400**, 2070
- Tully R. B., Courtois H. M., Sorce J. G., 2016, *AJ*, **152**, 50
- Vazdekis A., Sánchez-Blázquez P., Falcón-Barroso J., Cenarro A. J., Beasley M. A., Cardiel N., Gorgas J., Peletier R. F., 2010, *MNRAS*, **404**, 1639
- van Velzen S., et al., 2016, *Science*, **351**, 62
- van Velzen S., Holoiën T. W. S., Onori F., Hung T., Arcavi I., 2020, *Space Sci. Rev.*, **216**, 124
- Wevers T., van Velzen S., Jonker P. G., Stone N. C., Hung T., Onori F., Gezari S., Blagorodnova N., 2017, *MNRAS*, **471**, 1694
- Wevers T., et al., 2019, *MNRAS*, **488**, 4816
- Wright E. L., et al., 2010, *AJ*, **140**, 1868
- Zabludoff A., et al., 2021, arXiv e-prints, p. [arXiv:2103.12150](https://arxiv.org/abs/2103.12150)

APPENDIX A: ADDITIONAL MATERIAL

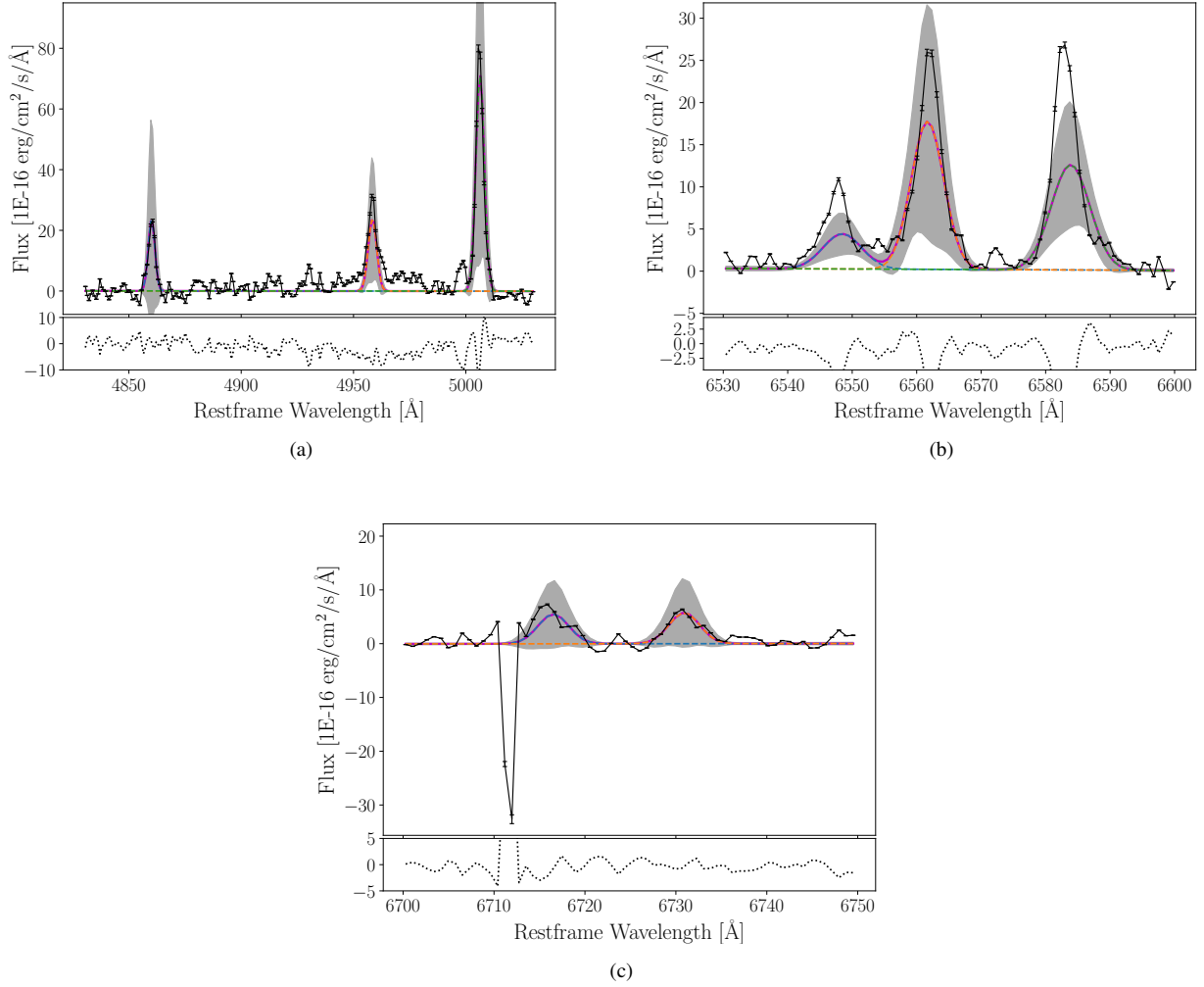


Figure A1. Fit to the emission lines of NGC 3599 after subtracting the starlight component of the host galaxy spectrum. The data are shown in black, the total best fit is shown in magenta, the individual components have varying colours. (a) shows $H\beta$ (blue) and $[O\text{ III}]\ \lambda 4959$ (orange) and $\lambda 5007$ (green), (b) shows $H\alpha$ (orange) and $[N\text{ II}]\ \lambda 6548$ (blue) and $\lambda 6584$ (green) and (c) shows $[S\text{ II}]\ \lambda 6717$ (blue) and $\lambda 6731$ (orange). Error bars to the spectrum are indicated in all frames in black, the grey shaded area corresponds to the 3σ region of the best fit.

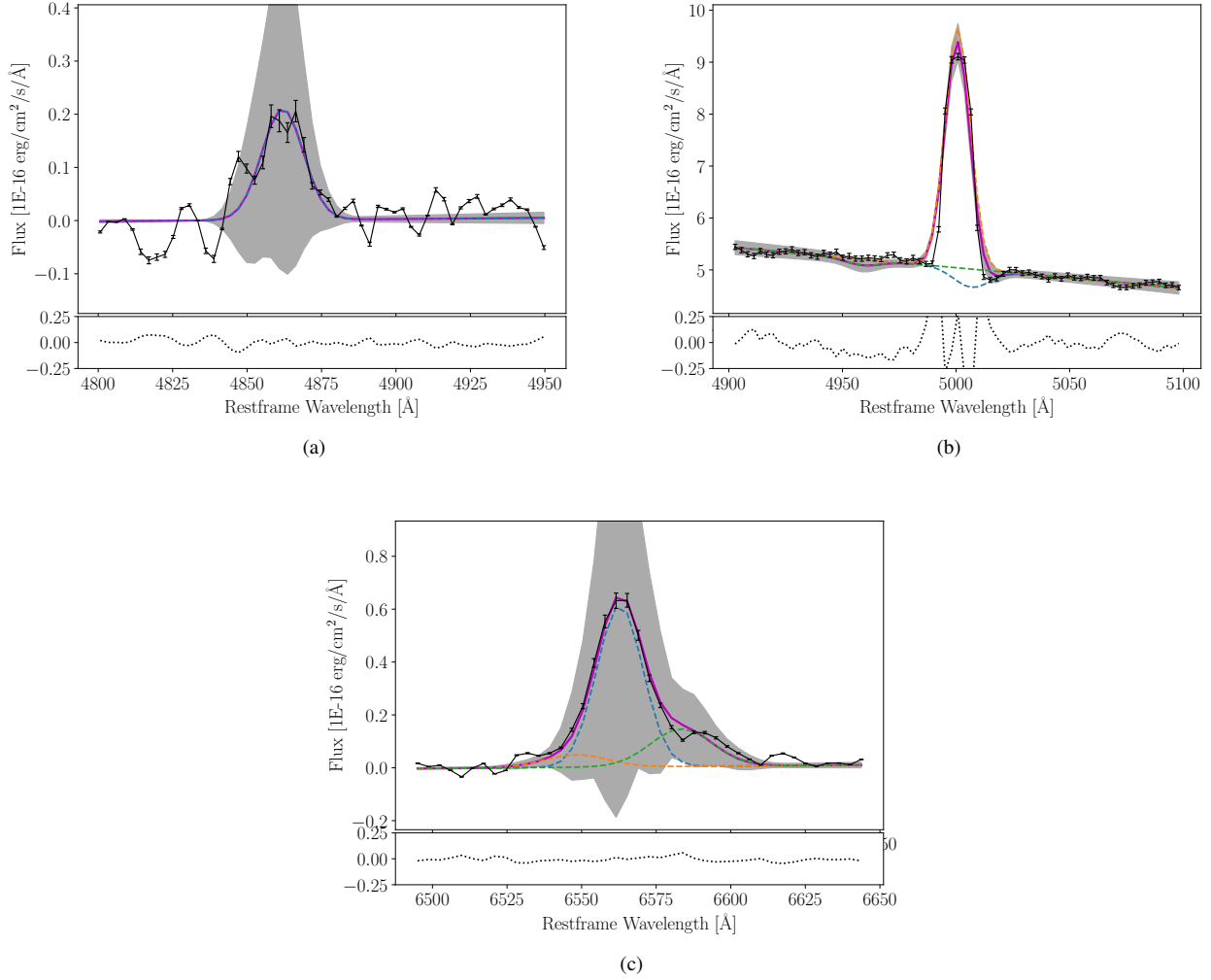


Figure A2. Fit of the emission lines of the hosty galaxy of PTF09axc with the starlight component subtracted for (a) and (c) and without the background or the starlight component subtracted for (b). The data are shown in black, the total best fit is shown in magenta, the individual components have varying colours. (a) shows $H\beta$ (blue), (b) shows $O\text{I } \lambda 5577$ terrestrial skyline (orange) and $[\text{O III}] \lambda 4959, 5007$ line (green and blue respectively) and (c) shows $H\alpha$ (blue) and $[\text{N II}] \lambda 6548, 6584$ (orange and green respectively). Error bars to the spectrum are indicated in all frames in black, the grey shaded area corresponds to the 3σ region of the best fit.

Table A1. Results of line fitting of the most prominent emission lines in the host galaxy nuclear spectra of TDE candidates XMMJ1115 and PTF09axc.

source	WL [Å]	[O III] $\lambda 4959$		WL [Å]	[O III] $\lambda 5007$	
		FWHM [km s ⁻¹]	flux [1E-16 erg cm ⁻² s ⁻¹]		FWHM [km s ⁻¹]	flux [1E-16 erg cm ⁻² s ⁻¹]
XMMJ1115	4958.4±0.3 [†]	270.0±27.8*	112.45±34.36	5006.3±0.3 [†]	267.5±27.5*	337.35±103.07
PTF09axc	<i>4958.94±0.00[†]</i>	<i>774.17±0.00*</i>	0.46	<i>5006.84±0.0[†]</i>	<i>766.77±0.0*</i>	1.39
source	WL [Å]	H β		WL [Å]	H α	
		FWHM [km s ⁻¹]	flux [1E-16 erg cm ⁻² s ⁻¹]		FWHM [km s ⁻¹]	flux [1E-16 erg cm ⁻² s ⁻¹]
XMMJ1115	4860.1±0.4	215.9±30.2	87.80±43.17	6561.7±0.3	272.8±24.6	111.48±30.31
PTF09axc	4861.9±2.1	605.3±200.1	2.18±1.24	6562.8±1.9 [‡]	569.9±219.1	8.14±4.57
source	WL [Å]	[N II] $\lambda 6548$		WL [Å]	[N II] $\lambda 6584$	
		FWHM [km s ⁻¹]	flux [1E-16 erg cm ⁻² s ⁻¹]		FWHM [km s ⁻¹]	flux [1E-16 erg cm ⁻² s ⁻¹]
XMMJ1115	6547.5±0.3 [‡]	324.0±25.1**	31.32±6.49	6583.9±0.3 [‡]	322.2±25.0**	93.95±19.48
PTF09axc	6548.1±0.0 [‡]	950.2±197.8**	1.04±0.47	6583.5±1.9 [‡]	945.1±196.8**	3.13±1.41
source	WL [Å]	[S II] $\lambda 6717$		WL [Å]	[S II] $\lambda 6731$	
		FWHM [km s ⁻¹]	flux [1E-16 erg cm ⁻² s ⁻¹]		FWHM [km s ⁻¹]	flux [1E-16 erg cm ⁻² s ⁻¹]
XMMJ1115	6716.5±0.3 ⁺	177.1±24.3 ⁻	23.28±9.08	6730.9±0.3 ⁺	176.8±24.2 ⁻	24.37±9.28
PTF09axc

Note. With ... we indicate that this line could not be fitted to the data. Different markers indicate quantities that were tied to the same value (FWHM) or a set separation (WL) for each of the sources. Numbers in italics were forced to the mentioned value to obtain a 2σ upper limit (UL) on the flux of that emission line. Flux measurements without error are 2σ upper limits.

This paper has been typeset from a $\text{\TeX}/\text{\LaTeX}$ file prepared by the author.